Fiber Optic Sensor Prototype for Breast Cancer Imaging

THE OHIO STATE UNIVERSITY

Honors Thesis

Adam Bangert

May 19th, 2006

Advisors:

Professor Allen Yi, Industrial, Welding and Systems Engineering Department

Professor Ronald Xu, Biomedical Engineering Department

Abstract

Breast cancer is the most common type of cancer and the second most common cause of death by cancer for women. Early diagnosis of a malignant tumor in the breast can dramatically increase survivability. Therefore, the clarity and accuracy of a detection scheme is crucial to improve the survival rate of breast cancer. Near-Infrared Diffuse Optical Imaging and Spectroscopy (NIR-DOIS) is an imaging methodology under development which has the potential to clearly and accurately assess the malignancy of a suspicious lesion. Tumor malignancy corresponds to certain physiological parameters, namely oxygen saturation and hemoglobin concentration. NIR-DOIS is capable of measuring these parameters, providing a functional measurement of multiple physiological parameters with potential molecular sensitivity. When compared with other imaging modalities, NIR-DOIS has the advantage of being a low cost, non-invasive, real-time diagnostic.

This imaging technique can be accomplished using fiber optic cables which are arrayed in a hand-held sensor head that is placed against the skin of the patient. The near-infrared light shines from the source fiber into the tissue and the reflected light is collected by the detector fibers. Source and detector fibers are connected to a tissue oximetry device that synchronizes the light illumination and the data collection, allowing it to interpret physiological parameters such as oxygen saturation and hemoglobin concentration from optical measurements. In order to reconstruct the embedded tissue heterogeneities such as breast tumors, it is necessary to collect multiple data sets with a matrix of sources and detectors. However, the fact that the existing tissue oximetry system has limited sources and detectors prevents the reconstruction of the tissue heterogeneities with high accuracy. In order to improve the imaging capability of the existing tissue oximetry system, it is necessary to develop an imaging head with a condensed distribution of source and detector channels, and an optical switching unit that can rapidly sweep through all these source and detector channels. The hypothesis of this project is that the optical switch will be an effective means to accurately detect oximetry data using NIR-DOIS.

The research project includes completing a prototype optical switch, programming the necessary motor control functions to integrate the switch with a computer, and testing the device to determine baseline performance and potential clinical efficacy. Performance

testing will be done using a laser and a light detector in order to determine light transmission through the optical switch, first through the fibers alone and then through the switch.

Introduction

This paper will discuss background information about breast cancer, current detection methods, and the utility of optical imaging. The prototype device will be described including the concept of the device, and its design, manufacture and operation. Next, experiments designed to test the performance of the device are discussed, including descriptions of the setup and methodology, as well as the data collected and the steps taken to normalize the measurement outputs.

Background

Breast cancer is the most common type of cancer and the second most common cause of death by cancer for women. The progress of cancer in the breast is broken down into five stages: Stage 0 indicates a small cluster of non-invasive cancer cells, Stage 1 indicates a tumor up to 2 cm in size with no spread, Stage 2 indicates that small tumors have spread to the axillary lymph nodes, Stage 3 indicates that tumors of any size have spread to the lymph nodes, and Stage 4 indicates metastases in other organs. Early diagnosis of a malignant tumor in the breast can dramatically increase survivability: over 95% of patients diagnosed with early breast cancer (stage 1 and 2) who have received treatment survive five years past their diagnosis [1, 2]. Therefore, *the clarity and accuracy of a detection scheme is crucial to improve the survival rate of breast cancer*. Currently, the most widespread detection scheme for breast cancer is X-ray mammography, which has the ability to distinguish features within the breast that have higher density than surrounding tissue. Increased mammographic density has shown strong correlation with risk factors that are important causes of breast cancer [3]. However, X-rays cannot detect any physiological parameters, have difficulty distinguishing varying tissue density in women with dense breast tissue, and can lead to health problems when overexposed to them [4].

Further complicating the use of X-ray mammography is the standardized method for interpreting mammograms. The Breast Imaging Reporting and Data System (BI-RADS) is an effort on the part of the American College of Radiology to use unambiguous language to

classify breast lesions on a 1-5 scale. A BI-RADS score of 1 indicates a negative mammogram, and a score of 5 indicates a lesion that is "highly suspected of malignancy" [5]. Overall, the mammograms evaluated with the BI-RADS system have high sensitivity (95%), but low specificity (9%), indicating that the test often returns a false positive. Of particular concern is the somewhat ambiguous BI-RADS score of 3, which indicates a lesion that is "probably benign." According to one study, the positive predictive value of a BI-RADS score of 3 was only 5%, meaning the rate of false positives is very high [6]. Since a positive mammogram can result in biopsy or lumpectomy, a false positive could therefore lead to unnecessary surgery and would carry with it the risks and costs associated with surgical procedures. For this reason, the need exists for an imaging technique to supplement mammography, self breast exam and clinical breast exam as a detection scheme which can determine with more certainty the malignancy of suspicious lesions. [7, 8]

Near-infrared diffuse imaging and spectroscopy (NIR-DOIS) is an imaging method under development which has the potential to detect the physiological properties of heterogeneities in tissue, as opposed to mammography, which detects physical properties. Since NIR-DOIS uses optical infrared radiation with much less energy than X-ray radiation, photons interact with the tissue, providing data on the light scattering, absorption, and fluorescence of the imaging medium. This can provide much more information about structure, biochemistry, physiology and molecular function than X-rays, whose high-energy photons follow an undisturbed path through the tissue. Unlike X-rays, near-infrared light only penetrates tissue on the centimeter scale, so its imaging utility is limited to detecting heterogeneities of interest which are near the skin. For this reason, near-infrared imaging is extremely useful in the field of breast cancer research.

The physiological properties which NIR imaging can extrapolate are oximetry data, or the properties of oxygen within the blood and tissues. Chromophores are molecules that absorb incident radiation and emit radiation of a specific frequency. By measuring the frequency of the emitted radiation when two light sources of known frequencies are incident upon a group of chromophores, the identity of each chromophore in a sample can be determined and its concentration quantified. Among the many chromophores that can be detected by near-infrared light are oxygenated hemoglobin and de-oxygenated hemoglobin because they are the major sensitive light absorbers in blood (see figure 1). Hemoglobin is

the protein found in red blood cells which carries oxygen from the lungs to the tissues and carbon dioxide back again to the lungs. The two wavelengths of light used in this study were 690 nm and 830 nm, which elicit very different responses in the chromophores. The graph in figure 1 shows the extinction coefficient, or a measure of how much light is absorbed, as a function of light wavelength. The behavior of deoxy-hemoglobin and oxy-hemoglobin are shown under different incident light wavelengths. The concentration of each chromophore can be calculated if the extinction coefficients and absorption coefficients are known for both chromophores and both wavelengths, as shown in the equations listed below. By measuring the relative concentrations of oxygenated hemoglobin (HbO) and de-oxygenated hemoglobin (Hb), oxygen saturation (SO_2) can be calculated [9].

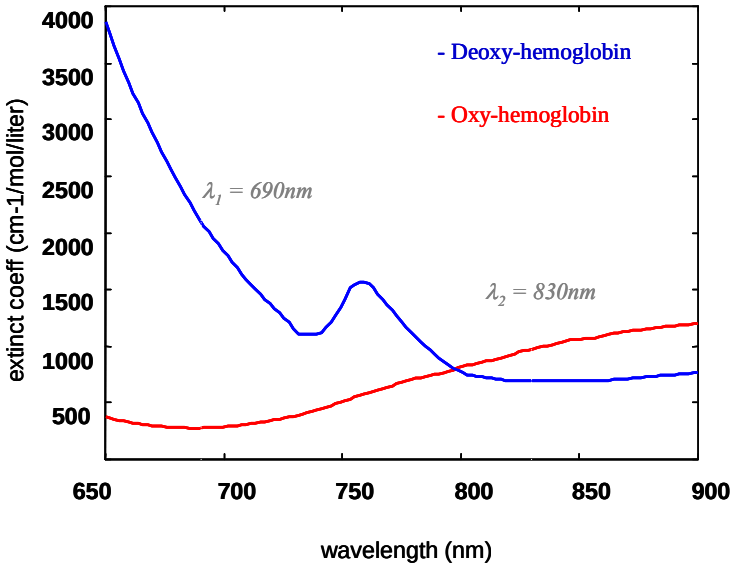

$$[\mathrm{Hb}] = \frac{\varepsilon_{HbO}^{\lambda 2}\mu_a^{\lambda 1} - \varepsilon_{HbO}^{\lambda 1}\mu_a^{\lambda 2}}{\left(\varepsilon_{Hb}^{\lambda 1}\varepsilon_{HbO}^{\lambda 2} - \varepsilon_{Hb}^{\lambda 2}\varepsilon_{HbO}^{\lambda 1}\right)}$$

$$[\mathrm{HbO}] = \frac{\varepsilon_{Hb}^{\lambda 1}\mu_a^{\lambda 2} - \varepsilon_{Hb}^{\lambda 2}\mu_a^{\lambda 1}}{\left(\varepsilon_{Hb}^{\lambda 1}\varepsilon_{HbO}^{\lambda 2} - \varepsilon_{Hb}^{\lambda 2}\varepsilon_{HbO}^{\lambda 1}\right)}$$

$$[HbT] = [Hb] + [HbO]$$

$$SO_2 = \frac{[HbO]}{[HbT]}$$

Figure 1: Light attenuation of two chromophores as a function of incident light wavelength [10]

Oximetry data are of interest because tissue heterogeneities like cancerous tumors exhibit altered physiology with respect to oxygen saturation and hemoglobin concentration. Cancer is a genetic disease in which regular cell cycle signaling is somehow compromised, and excessive proliferation and longevity of cells occurs. The rapidly dividing cells must be nourished at an equally rapid rate because of their increased metabolism, so hastily created vasculature perfuses tumor regions. Cancerous tumors have a higher hemoglobin concentration due to increased vascularity, and lower oxygen saturation due to increased metabolism. Near-infrared imaging has the capability to more accurately diagnose the

malignancy of suspected cancerous tumors because it can determine oxygen saturation and hemoglobin concentration [11-13].

Prototype Concept

In order to create a device that can accurately measure oximetry data over a large area, near-infrared light must be transmitted to the tissue, and reflected light must be collected and measured by many detector channels. Measuring a data set over a large area with a condensed matrix of many detectors will serve two important functions. The first is that the density of detector fibers will create a data set with high resolution and accuracy. The second is that the location of heterogeneity can be calculated based on the perturbation of specific detectors in the array. Knowing which detectors in the array returned abnormal values will make it possible to identify the x-y location of the abnormality. The large detector region with a dense array of detector fibers will allow for the two-dimensional characterization of physiological heterogeneities.

In this prototype, micro fiber optic cables were used to transmit the light from the light source to the breast and back again to the detector. Light first travels from a light source to a sensor head, a plastic disk that can be seen in figure 3. The light source is the larger φ2 millimeter fiber shown in the center of the disk. The reflected light is then collected by the smaller φ0.5 millimeter fibers that surround the light source fiber. The light collector fibers are arrayed in twenty separate groups of four that form radii on the disk. The light source/detector device only has inputs for four detectors, but to produce a two-dimensional data set with acceptable accuracy and resolution, many detector channels are required. Therefore, the condensed matrix of detector channels must be arranged so that each group of four light detector fibers can be measured in rapid succession. To accomplish this, an optical switching unit that can rapidly sweep through all these detector channels was necessary. Similar experiments using near-infrared light have shown efficacy in detecting heterogeneities in the breast, but without the use of optical switching units. It is the hope of this project that the matrix of detector fibers and the optical switching unit will have higher sensitivity in detecting embedded abnormalities by creating a larger data set, and will have higher resolution due to the high density of detector fibers on the sensor head [14].

The optical switch consists of a large plastic disk and a rotating arm (see figure 4). It is powered by a step motor inside the large plastic disk. As the rotating arm sweeps past the array of light source fibers on the disk, it brings the fibers on the arm into contact with the fibers on the disk, allowing the signal of reflected light to pass from the disk to the arm. From the arm, the fibers lead to the detector device which transduces the light measurement into a voltage signal. The hypothesis of this project is that the optical switch will be an effective means to create an accurate image using NIR-DOIS.

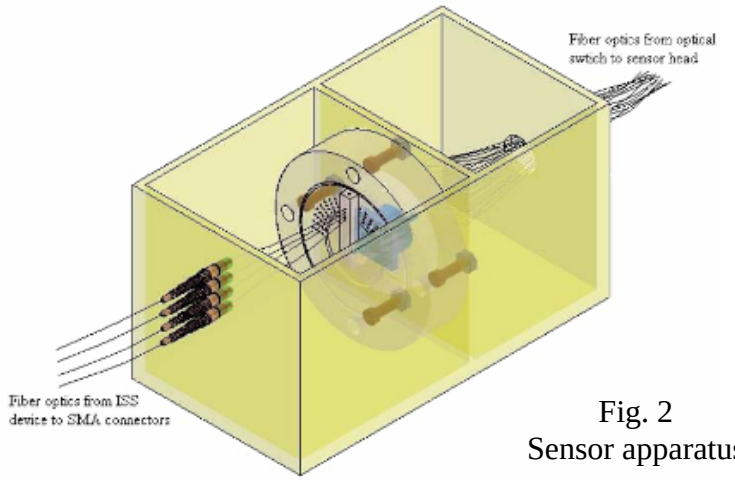

Fig. 2
Sensor apparatus

Design and Manufacture

The components of the NIR-DOIS device described above require a high degree of precision in their manufacture. In order to attain an acceptable level of light transmission and signal clarity, tight tolerances must be held, and surface properties must be taken into careful consideration. For the fibers to transmit light effectively, their terminal surfaces must be highly polished and normal to the fiber. This is accomplished by loading each fiber into a metal polishing disk, which secures the fiber using a set screw (see figure 5). The disk ensures that the fiber face is perpendicular to the fiber so that light does not refract when it meets an air interface. The fiber is polished using increasingly finer paper, from 5 micron to 0.3 micron grit paper. After polishing, the fiber ends are viewed using a fiber inspection scope to determine the surface characteristics. The magnification power of the scope is 200, so any surface properties beyond that scale are not measured, and assumed not to affect the functionality of the fiber. This precision is necessary to ensure that the light source signal or reflected light signal is not compromised.

Major components of the device are manufactured out of a clear acrylic plastic, poly-methyl-methacrylate (PMMA). PMMA is frequently used in optical applications due to its clarity, hardness, stiffness and machinabilty. These properties also make it suitable for structural applications, as in the case of this device. Furthermore, the transparency of the device housing allows for easy inspection of its functions and construction.

The PMMA components were machined on a high-precision CNC machining center. There are six flat rectangular pieces that comprise the walls of the device, a circular sensor head (figure 3), a large disk that is the body of the optical switch, and a rotating arm that sweeps between detector channels (figure 4). The walls of the device are held together with 5/32nd inch bolts. The large disk is mounted vertically on the interior wall with four 5/16th inch bolts. The step motor that controls the rotating arm is mounted to the inside of the large disk, and is secured by four #4-40 screws. The rotating arm is press-fit onto the 5 mm diameter rotating shaft of the step motor (see figure 4).

Fig. 3: Sensor Head

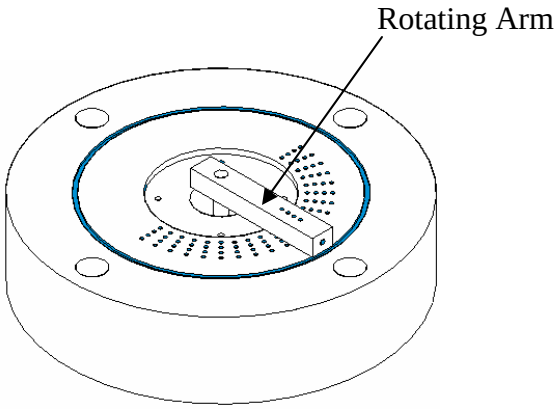

Fig. 4: Optical Switch Body

In addition to the necessary precision of structural components, other portions of the device that demand precision engineering are the fiber interface regions. For clarity, in order to distinguish between the two sides of the optical switch, the sides will be called the patient side or the detector side. The large disk comprises the patient side of the optical switch, and the rotating arm comprises the detector side of the switch. As shown in figures 2-4, fibers insertion points in the PMMA device components are in the sensor head, the patient side of the optical switch, and the rotating arm on the detector side of the optical switch. At each interface, the polished fibers must be precisely arranged to ensure signal

clarity. On the sensor head, and both sides of the optical switch, the fibers are jacketed with simple cylindrical stainless steel ferrules. This adds strength and rigidity to the interface. At the interface with the light source and with the detector device, the fibers terminate in a standard SMA connector. This common connector is found in many other optical applications. Like the fibers which terminate in steel ferrules, the tips of the SMA-terminated fibers were also carefully polished to a precise surface finish (see figure 5).

Fig. 5: Polishing Fibers with SMA Tip (left) and Ferrule Tip (right)

Three different fiber diameters, and thus three different types of fiber ends, were used in the construction of this device. The fiber leading from the light source to the sensor head is the largest of the three sizes, at φ2 millimeters (.080 inch). The large diameter of the light source fiber allows for powerful transmission of light and good penetration into the tissue. There were no SMA connectors readily available with a φ2 mm inner diameter, so one was fabricated using a lathe and center drill. The two ends of the φ2 mm fiber are terminated by an SMA connector at the light source end and a φ4.75 mm ferrule at the sensor head end. The reflected light signal carried from the sensor head to the patient side of the optical switch is transmitted via φ0.5 mm (.020 inch) fibers. These fibers are terminated by stainless steel ferrules on both ends which have outer diameters of φ1/16th inch (1.59 mm). The signal carried from the detector side of the optical switch to the oximetry device is transmitted through φ1.0 mm diameter fibers (.040 inch). The ends of the fibers that insert into the detector side of the optical switch are also terminated by steel ferrules. Like the other ferrules, they have an outer diameter of φ1/16th inch (1.59 mm), but a larger inner diameter to accommodate the larger fiber. These larger ferrules were not anticipated in the original design, and modifying the existing ferrules to expand the inner diameter was impractical. Stainless steel capillary tubing that had nearly the correct dimensions was ordered, and cut

into small segments using a wire EDM process to eliminate crimping or burr formation. The ends of the φ1.0 mm fiber are terminated by an SMA connector at the oximetry device and a ferrule on the detector side of the optical switch.

The reflected light signal is transmitted from a smaller fiber (φ0.5 mm) to a larger fiber (φ1.0 mm). By creating the interface in this manner, it is assured that there will be no signal loss. Were the interface to transfer from a larger to a smaller fiber, there would be more signal area than available surface area, and some of the signal would be lost. Furthermore, providing a large "target" for a small area of light allows some small room for error in fiber alignment (see figure 6).

The large disk of the optical switch, the sensor head and the rotating arm all required precision holes to be drilled in them in order to accommodate the ferrule-tipped fiber ends. The holes needed to be accurate in size, location and arrangement relative to each other. On the sensor head, there are eighty φ1/16th inch holes arranged in twenty separate radial groups of four holes each (see figure 3). In the center of the sensor head there is a larger hole with diameter φ4.75 mm to accommodate the φ2 mm fiber and its ferrule tip. In order to create an accurate image, the radial groups of four needed to have a consistent angle between them. On the sensor head, the groups are spaced 18 degrees apart and were machined to an accuracy of 5 arc seconds.

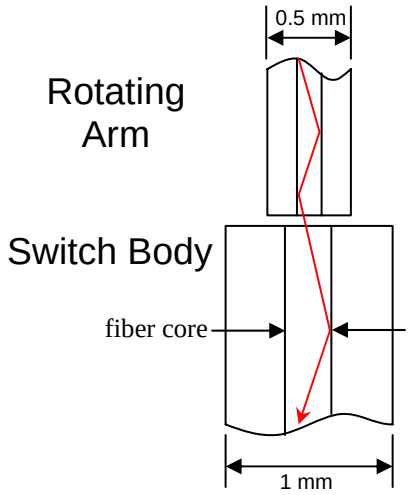

Figure 6: Light Transmission Through Switch

On the large disk body of the optical switch, twenty groups of φ1/16th inch holes are also present. However, they are arrayed in a semi-circle instead of a full circle, creating a spacing of 9 degrees between each radial group. The stepper motor inside the large disk body of the optical switch sweeps the rotating arm across this 180 degree array of holes. To avoid twisting the fibers that extend from the rotating arm to the detector device, the rotating arm sweeps back and forth across the 180 degree range, instead of a continuous 360 degree motion. To require the holes to not only have an accurate size and position, but also to be precisely located with respect to one another in both Cartesian and polar space, adds another

degree of precision to the design. These holes were also created to an angular accuracy of 5 arc seconds, and a Cartesian accuracy of 2-3 micron.

Motor Operation

Even with precisely located holes, the device would not function as intended without a precision stepper motor. Since the motor is not designed to run continuously, a stepper motor is more appropriate for this device than a continuous rotary motor. The motor and controller that were chosen use a 12 volt DC input and are controlled by a serial port on a computer. The 5704 series high accuracy motor, purchased from Lin Engineering, is handled by the R164 Single Axle Controller from RMS Technologies, and has a resolution of 0.45° for precise control. From the computer, inputs such as position, velocity, acceleration and coordinate information can be entered. The stepper motor, as its name implies, can be moved a given number of steps in order to reach a certain position. One full revolution of the motor is 800 steps, and because the holes on the optical switch are spaced 9 degrees apart, the move from one group of four holes to the next is a 20 step movement.

To add another degree of reliability, precision and repeatability, an optosensor was added to the optical switch assembly. The optosensor is an optional add-on to the RMS Technologies Controller as part of the Designer's Kit. The rotating arm has a groove running longitudinally down its length (groove not pictured in figure 4), which coincidentally has a slightly smaller width than the body of the optosensor. The opto-sensor was mounted on the rotating arm with a press fit. The sensor itself creates a beam of light, which when broken sends a signal back to the motor controller. The RMS motor comes packaged with the optosensor and includes a command in its repertoire which can rotate the motor until the optosensor beam is broken (see Appendix 1). This command improves the repeatability of the motor because the motor can first find its zero coordinate before making any move. The optosensor beam is broken by a protruding arm, which was temporarily constructed out of a bent copper wire. There are three rows of extra holes drilled in the large disk of the optical switch, and the bent wire arm is located using these extraneous features. In future work, a more substantial and precise arm will be fabricated, and possibly located using the precisely located (but unnecessary) holes.

The arm is located at position zero, which does not contain any fibers. As discussed earlier, the distance between each position of the rotating arm is twenty motor steps, and that distance is extremely reliable because the holes were created on a high-precision CNC with a 5 arc-second angular accuracy. However, it was difficult to accurately locate the arm so that the beam of the optosensor was broken exactly at position zero. While it was possible to create position zero *approximately* twenty steps past position one (a situation in which every move would be exactly twenty steps), it was difficult to make it exact with the current setup. In order to compensate for this inaccuracy, a motor offset was added to the program. Before executing any move, the motor first zeroes itself using the optosensor and the bent piece of wire, and then moves the distance of the offset to position one. Once in position over the first group of fibers, each successive move is a consistent twenty motor steps.

A motor control program written using LabView software allows for the testing of individual fiber groups or for executing a loop program in which the rotating arm sweeps across all twenty fiber groups. The program communicates with the controller through the computer's serial port, and sends commands that can be seen in Appendix 1. The device can be controlled through HyperTerminal by inputting text strings line-by-line, or by automating the procedure using concatenated text strings via the LabView interface.

In order to test each individual fiber group, the LabView program reads an input position, moves the arm back until the optosensor is interrupted, and then moves the arm to that position with the desired velocity and acceleration. Because this sensor will be used to study living tissue, it needs to take its reading rapidly to account for the rapidly changing biological environment that is created with each heartbeat. This is especially true in the study of blood oximetry, because hemoglobin varies greatly with systolic and diastolic blood pressure. However, though the light reading can take place very quickly, it is not instantaneous. The arm will need to briefly pause at each fiber group to take its reading.

Light Source Operation

The light source and detector device, like the stepper motor, can be controlled via HyperTerminal by inputting text strings. The power level for each source can be set and the device can send data packages which include every source/detector combination. Similarly to the motor control program, these text strings can be entered automatically using LabView

software. Using a power set program written in LabView (see Appendix 1), all source power levels were set to 1000 for testing. Voltage measurements were written to text files for each test.

Experiment

Methodology

The first phase of testing the prototype was to quantify the performance of the device using homogeneous phantoms. The optical properties of the phantoms are summarized in Table 1. Four data points are of interest in quantifying the performance of the device: variability between light source channels, transmission efficiency, variability between fiber groups, and variability between detector channels. Understanding the inherent variability in the system will allow for accurate signal processing algorithms that can normalize data collected from the device.

		μa	μs
Phantom 1	690 nm	0.019	8.2
	830 nm	0.018	6.2
Phantom 2	690 nm	0.048	9.5
	830 nm	0.019	6.9
Phantom 3	690 nm	0.034	8.6
	830 nm	0.021	6.4

Table 1: Test Phantom Optical Properties

Offset

The first step in measuring the performance of the sensor was to determine the optimal offset value. The programmable offset, as mentioned under the Operation heading, is a variable "fudge factor" to ensure that the fibers on the arm are centered over the fibers on the switch body. First, the bent wire arm was affixed to the walls of the device using glue so that the beam of the optosensor would be broken approximately twenty steps past the first

fiber group. Next, the sensor head was placed on one of the phantoms, and readings were taken at motor position 2 with different offsets. When performing the test, the motor was zeroed and then moved the distance of the offset to reach position 1. Then, the motor moved twenty steps to position 2 and a reading was taken and recorded. Five sets of data were taken at each motor position in order to provide several data points. These data can be seen in Appendix 2. An offset of 19 steps was determined to be the optimal value because the average voltage readings collected from that location were the highest.

Gold Standard

In order to test the variability between light source channels, a benchmark was first established using a closed loop between the light source, a gel phantom and the light detector. This "gold standard" test was used to calibrate the device so that each of the 690 nm wavelengths and each of the 830 nm wavelengths were producing the same voltage signal. The test setup included a test bar, the light source and a gel phantom. The test bar was fabricated to simulate the dimensions of the sensor head (see figure 7). While the actual sensor head could have been used for this test, it was difficult to separate the fibers from it, so a simulated sensor head was created that could only accept four detector cables at once. Near-infrared light from the light source traveled down the φ2 mm fiber to the phantom, and reflected light was carried back to the detector via four 1 mm detector fibers. Only four detectors and one source channel could be used in the test bar so that each of the four sources could be tested individually. By varying only the light source and keeping the power level, phantom and channel the same, it was possible to isolate the effects of each light source. Sources 1 and 4 both emit a 690 nm wavelength light signal, and Sources 2 and 3 emit light with a wavelength of 830 nm. However, when set to the same power level, each source emits light with a slightly different power than its counterpart. These variations in power output are likely due to variations in the fibers inside the light source/detector device. Since a loss in power output can be expressed as a percentage of total power output, a

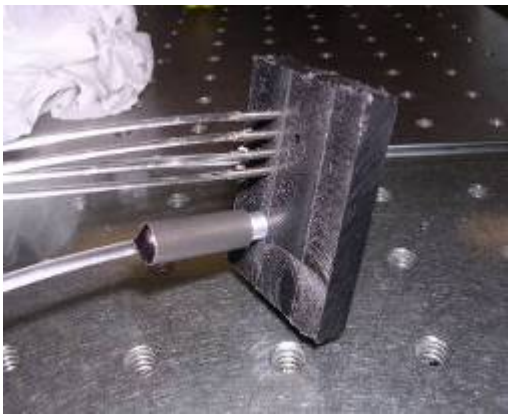

Fig. 7: Test Bar for Gold Standard test

multiplier constant would allow the voltage signal of one source to be calibrated to match its corresponding light source.

A total of 10 data points were taken at each combination of source and phantom, resulting in 12 sets of data. Each data set includes readings from all four detectors. The readings from each detector were compared to produce an average reading from each data set. Next, the corresponding light source averages were compared to each other; Source 1 was compared to Source 4, and Source 2 was compared to Source 3. In each case, a ratio was determined by dividing the larger value by the smaller value (see Appendix 3). These constants, which were all greater than 1, boosted the weaker signal to match the stronger signal.

Comparing the data across the phantoms, it was found that the average ratio did not vary much from phantom to phantom. For example, the ratio between Source 1 and 4 on the first detector had a variance of 0.000611 across all three phantoms. Similarly, the variance between readings taken from different phantoms is low for the 830 nm sources. While there is more variance between the phantoms for the 830 nm sources than between the phantoms for the 690 nm sources, the absolute variance is still two orders of magnitude less than the voltage readings. Furthermore, the ratio values from each of the detectors (D1-D4) are very similar. Therefore, it was decided that finding an average coefficient across the three phantoms for each source and detector combination was an appropriate way to compile these data.

Power Setting Calibration

Once the "gold standard" data was recorded, every motor position was tested in the same manner: first by zeroing the motor, moving it the offset distance, and then moving it to the given location. This test included data sets from all twelve combinations of light source and phantom, and each data set was comprised of twenty readings, one from each fiber group. The raw data was plotted by light source wavelength and by phantom, as shown in Appendix 3. The readings from fiber group five were consistently low in every source/detector combination, so that data was removed from the test as an assignable cause variation, and was replaced by an average of the readings from fiber groups 4 and 6. While

no obvious discontinuity was found when that fiber group was inspected, it is possible that there is a broken or cracked interface, or that there is some crazing in the length of the fiber.

Ideally, the voltage measurement from each corresponding pair of detectors (e.g. detector 1 from light source 1 and 4) should have the same value. However, the inherent variance in the power output of corresponding sources separates the readings from the corresponding sources by some percentage. The graphs illustrate two things about the unfiltered data: first, the light source power outputs from corresponding light sources are not equal (the separation between readings from the same detector on corresponding light sources), and second, there is variance in the readings from different fiber groups (the waviness of the graphs).

The power calibration coefficients which were determined in the "gold standard" test were applied to the weaker light sources in each corresponding pair. The values from light source 1 were multiplied by the coefficients in Appendix 3 so that they would match the values of source 4, and the values from source 2 were increased to match the values from source 3. However, the graphs did not match up well; there was still a discrepancy between the measurements from the detectors from corresponding sources. In an effort to correct this failed adjustment, new power normalizing coefficients were calculated using data from the optical switch test. These new coefficients can be seen in Appendix 4. When the new coefficients were applied to the raw data, the detector readings from the corresponding sources showed much more comparable values (see Appendix 4).

Fiber Group Normalization

Once the power outputs of the light source device were calibrated, the next step in processing the device's output measurements was to correct for differences in readings from different fiber groups. As shown in Appendix 4, there is inherent variability between fiber groups as illustrated by the "spikiness" of the graphs. Since the device was constructed over an extended period of time by two different people, there could be slight inconsistencies in the method of attaching fiber ferrules using epoxy, securing fiber tips into the plastic device components, or polishing the fibers. Variations in the terminal surface of a fiber could affect its light transmission efficiency. Because the loss in transmission can be expressed as a percentage of total efficiency, it is appropriate to use a multiplier constant to correct the

discrepancies between fiber groups. Normalizing the outputs will smooth the curves so that there is little variation between the 20 fiber groups.

Once the raw data was modified to account for power output calibrations, it was examined further to find a method to normalize the readings from each fiber group. Again, since there was little variation between the phantoms, calculating averages was determined to be an appropriate way to compare the data. Algebraically, the average reading of the 20 fiber groups was calculated for each source/phantom combination. A "master average set" for each light source was calculated to find an average value across all three phantoms. Each point was compared against this "master average" and a ratio was calculated. Then, since the ratios of each data point to the "master average" were extremely comparable across the phantoms (based on low variances), a matrix was created for each light source which consisted of average ratios. The fiber group normalization coefficients are summarized in Appendix 5.

Graphically, this meant finding the horizontal regression line for each "spiky" line on each graph, and then finding the ratio between each data point and the regression line. Next, each data point is multiplied by that ratio to smooth the curve. Instead of finding a different average for each detector from each source from each phantom, an average of averages was calculated in an effort to make the coefficients independent of the imaging subject's optical properties.

Once applied to the data that was modified to account for power output calibrations, the averaged coefficient matrices demonstrated the ability to smooth the curves. The graphs with the normalized fiber groups can be found in Appendix 5. It is important to note that since the detector channels have not yet been normalized to account for decreasing light intensity, there are still distinct bands on the graphs.

Detector Channel Normalization

The variability between detector channels was determined using the data collected in the optical switch test. Not surprisingly, the detector channel that was nearest to the light source always returned the highest voltage value, and the detector channel farthest from the light source always returned the lowest value. This phenomenon is illustrated in Appendix 6,

a graph that plots the average reading of each detector. Like the other signal processing techniques, the detector readings will be linearized by boosting the measurements of the more distant detectors to match the detector nearest the light source.

It is extremely necessary to linearize the detector measurements because if the detector channels do not all return the same value in a homogeneous phantom, then the device will be unable to detect any type of heterogeneity in future tests. Therefore, the detector channels need to be normalized so that regardless of the phantom, they all return the same value when the phantom is homogeneous.

In order to compensate for the light attenuation that results from the changes in distance from light source to detector, an average constant was sought that would normalize the outputs from the different detector channels regardless of which phantom was being imaged. For each light source/phantom combination, the ratio of detector 1 (closest to the light source) to each of the other detectors was calculated. Again, the values of the ratio were very comparable, and their variances were small enough to consider using an arithmetic mean to find the average ratio of each combination of detectors. The ratios can be seen in Appendix 6 along with the detector channel normalized graphs. Once the coefficients were used to adjust the smoothed graphs, the distinct bands disappeared and the lines converged into a small range. Without normalizing the detector outputs, it would be impossible to know if a variation in a detector's reading were due to an embedded heterogeneity or simply due to the detector's distance from the source fiber.

Discussion

The tests described above resulted in several coefficient matrices that modify the raw data from the device and process into a usable signal that is capable of distinguishing heterogeneities. The first matrix is used to calibrate the outputs with respect to the power level of each light source. The second matrix smoothes the outputs of the device so that all twenty fiber groups are approximately equal. The third matrix normalizes the detector readings to account for the attenuation of the light source in the gel phantom. Each matrix is broken down by light source and detector, but remains independent of the optical properties of the phantom. This was accomplished by using average values in the normalizing

calculations. In each case, low variances between the values from each phantom motivated the use of averaging.

After all the signal processing steps, the data was confined to a small range on the graphs. The range was calculated by subtracting the minimum value from the maximum value within each source/phantom combination. In order to detect heterogeneities, the noise level must be low and the sensitivity of the sensor must be high. Table 2 summarizes the noise levels, expressed as percentages, of each source/phantom combination. Future testing will determine if the noise levels are acceptable for detecting heterogeneities with optical properties similar to cancerous tumors.

	Source 1	Source 2	Source 3	Source 4
Phantom 1	48.32%	48.32%	7.85%	15.62%
Phantom 2	22.92%	22.92%	18.15%	16.51%
Phantom 3	17.09%	17.09%	8.97%	8.24%

Table 2: Noise Levels after Signal Processing

Conclusions and Future Work

This paper has presented work in the fabrication and performance testing of a micro-fiber optical imaging system. Once the fabrication and construction of the device was complete, tests were conducted to measure the efficiency and variability of the device and its inputs and outputs. Based on these tests, the light source channels were calibrated to provide the same light signal to the tissue, the fiber groups were normalized to account for variation inherent in the device, and the detector channels were normalized to return similar values in a homogeneous phantom. The processed data indicates that the calibration and normalization algorithms worked for this data set; however some outliers in the raw data that affect the noise level and may disappear if another test is run. After quantifying the performance of the device and normalizing its inputs and outputs to account for variation, the next step will be to run another set of tests using the coefficients that were calculated from the first set of tests to see if they normalize the measurements appropriately. Once the coefficients are verified,

then experiments will be performed to test the device's ability to recognize heterogeneities based on oximetry data. This will be accomplished using gel phantoms with embedded heterogeneities which have optical properties that mimic the physiological properties of cancerous tumors. While this test will be initially done by examining the raw data of voltage signals, in the future, a graphical algorithm may be employed to create a two-dimensional image of the physiological functions in the imaged tissue.

Bibliography

1. Breast Cancer Facts & Figures 2005-2006: Atlanta: American Cancer Society, Inc
2. Breast Cancer Types. The Susan G. Komen Breast Cancer Foundation. Item No. 806-369. 2005.
3. Boyd, N.F., L.J. Martin, et al., Mammographic densities as a marker of human breast cancer risk and their use in chemoprevention. Curr Oncol Rep, 2001. 3(4): p. 314-21.
4. L. Liu, ''Breast cancer overview,'' Oncolink, University of Pennsylvania Cancer Center, 1999.
5. Breast imaging reporting and data system (BI-RADS). American College of Radiology, 1998.
6. A. Mendez, F. Cabanillas*, M. Echenique, K. Malekshamran, I. Perez & E. Ramos. Mammographic features and correlation with biopsy findings using 11-gauge stereotactic vacuum-assisted breast biopsy (SVABB). Annals of Oncology 14: 2003. p .450–454,
7. Shah, N., A. Cerussi, et al., Noninvasive functional optical spectroscopy of human breast tissue. Proc Natl Acad Sci USA, 2001. 98(8): p. 4420-5.
8. Li D, Meaney P, Tosteson T, Jiang S, Kemer T, McBride T, Pogue B, Hartov A, Paulsen K. Comparisons of three alternative breast modalities in a common phantom imaging experiment. Med. Phys. 30 .8., August 2003: p. 2194-2205.
9. V Ntziachristos, B Chance. Probing physiology and molecular function using optical imaging: applications to breast cancer. Breast Cancer Res 2001, 3: p. 41–46.
10. Xu, Ronald. "Biomedical Imaging and Tissue Oximetry by Near Infrared Light." ISE H694/821. The Ohio State University, Columbus, OH. 28 Mar. 2006.
11. Xu, R.X.; Bo Qiang; Olsen, J.O.; Povoski, S.P.; Yee, L.D.; Mao, J. Localization and Functional Parameter Reconstruction of Suspicious Breast Lesion by Near Infrared/Ultrasound Dual Modal Imaging. 27th Annual International Conference of the Engineering in Medicine and Biology Society, 2005. IEEE-EMBS 2005. 01-04 Sept. 2005: p. 4473 – 4476.
12. S. Srinivasan, B. Pogue, S. Jiang, H. Dehghani, C. Kogel, S. Soho, J. Gibson, T. Tosteson, S. Poplack, K. Paulsen. In Vivo Hemoglobin and Water Concentrations, Oxygen Saturation, and Scattering Estimates From Near-Infrared Breast Tomography Using Spectral Reconstruction. Acad Radiol 2006; 13:195–202.
13. X. Cheng, J. Mao, R. Bush, D. Kopans, R. Moore, and M. Chorlton. Breast cancer detection by mapping hemoglobin concentration and oxygen saturation. Applied Optics Vol. 42, No. 31, 1 November 2003: p. 6412-6421.
14. X. Cheng, X. Xu, S. Zhou, L. Wang, Bob Hu, F. Li, M. Wang. A Novel Optical Scanning System for Breast Cancer Imaging. Proceedings of SPIE Vol. 4244: 2001. p. 1605 7422.

Appendix 1

Start Character	Address	Commands	Run	End of a string
/	1-9*	Command strings	R	<CR>

Motor Command String Syntax

Command (Case Sensitive)	Operand	Description
		HOMING & POSITIONING
Z	0-max*	Initialize the Motor. Motor will turn towards 0 until the home opto sensor is interrupted. If already interrupted it will back out of the opto and come back in until re-interrupted. Current motor position is set to zero. Speed of homing is set by the 'v' command.
z	0-max*	Sets current position without moving motor
A	0-max*	Move Motor to Absolute position
f	0 or 1	Flag polarity. Sets polarity of home sensor, default is 0.
P	0-max*	Move Motor relative number of steps in positive direction. A value of zero will cause an endless forward move at speed 'V'. By doing so, it enters into Velocity Mode. Any other finite number will set the mode to be in Position Mode.
D	0-max*	Move Motor relative number of steps in negative direction (Note: Motor will not run in the negative direction if the position is at 0. You can use the 'z' command to set the 0 position to be further away in the negative direction.) A value of zero will cause an endless backwards move at speed 'V'. This will enter Velocity Mode. Any other finite number will set the mode to be in Position Mode.
T	-	Terminate current command
F	0, 1	Reverses the positive direction to be negative. The 'P' and 'D' command will reverse directions. Default is 0.
		VELOCITY & ACCELERATION
v	200-2500	In Position Mode, this sets the Start Speed of the Motor in half steps per second. This also sets the 'Z' command speed.
V	100-10000	In Position Mode, this sets the Top Speed of the Motor in half steps per second.
V	100-4000	In Velocity Mode, changes the Top Speed "on the fly".
c	300-900	In Position Mode, this sets the stop speed of the motor in half steps per second.
L	1-20	In Position Mode, this sets the Acceleration factor (acceleration = L*7500 steps/sec^2)

Motor Command Strings

Appendix 1

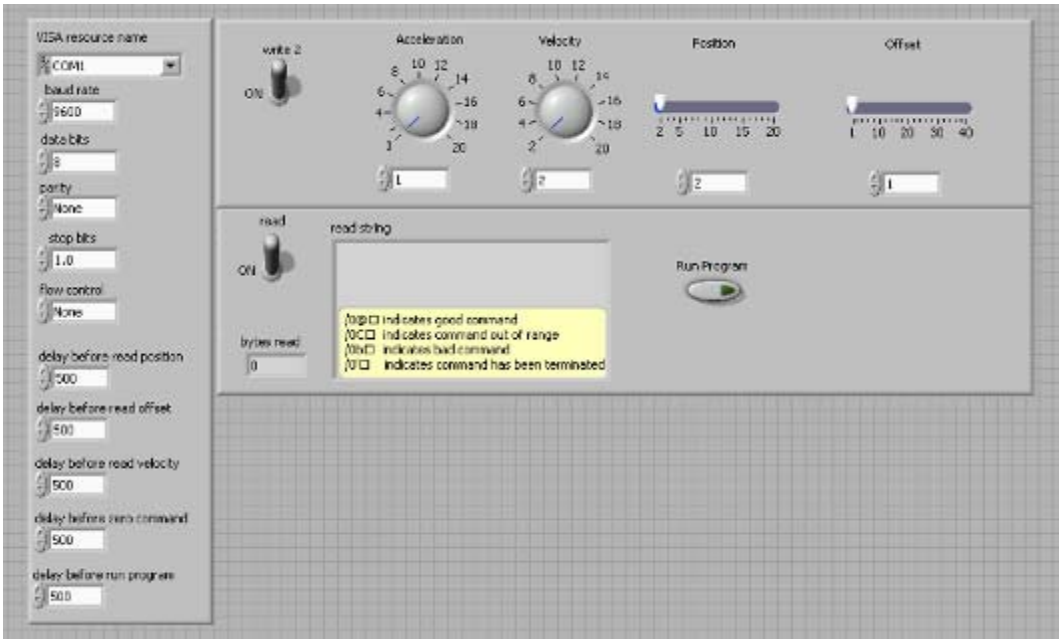

Front panel of LabView Motor Control Program

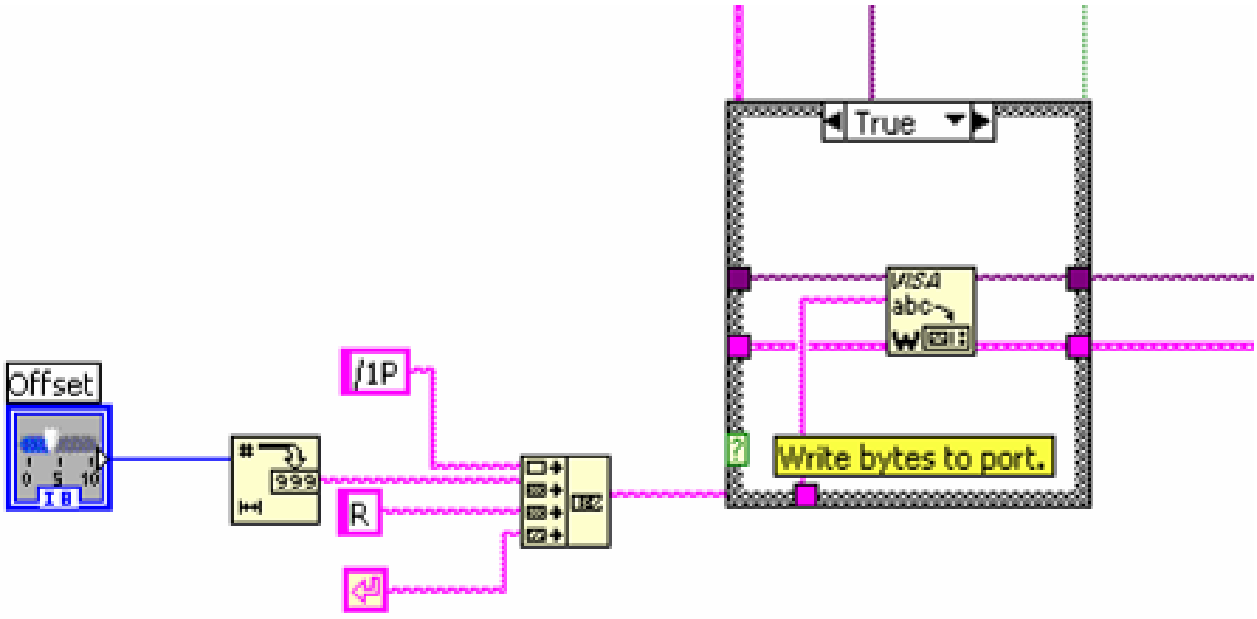

Block Diagram example of concatenated text string in LabView Motor Control Program

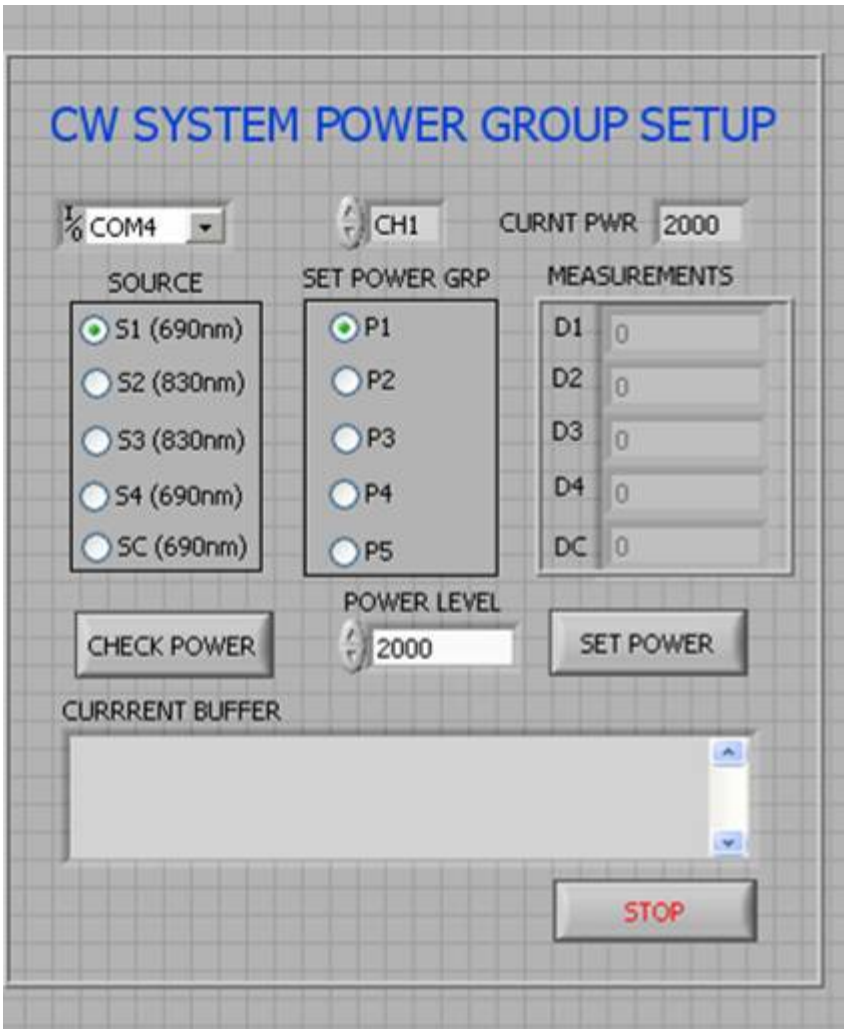

Front Panel of LabView Power Set Program

Appendix 2

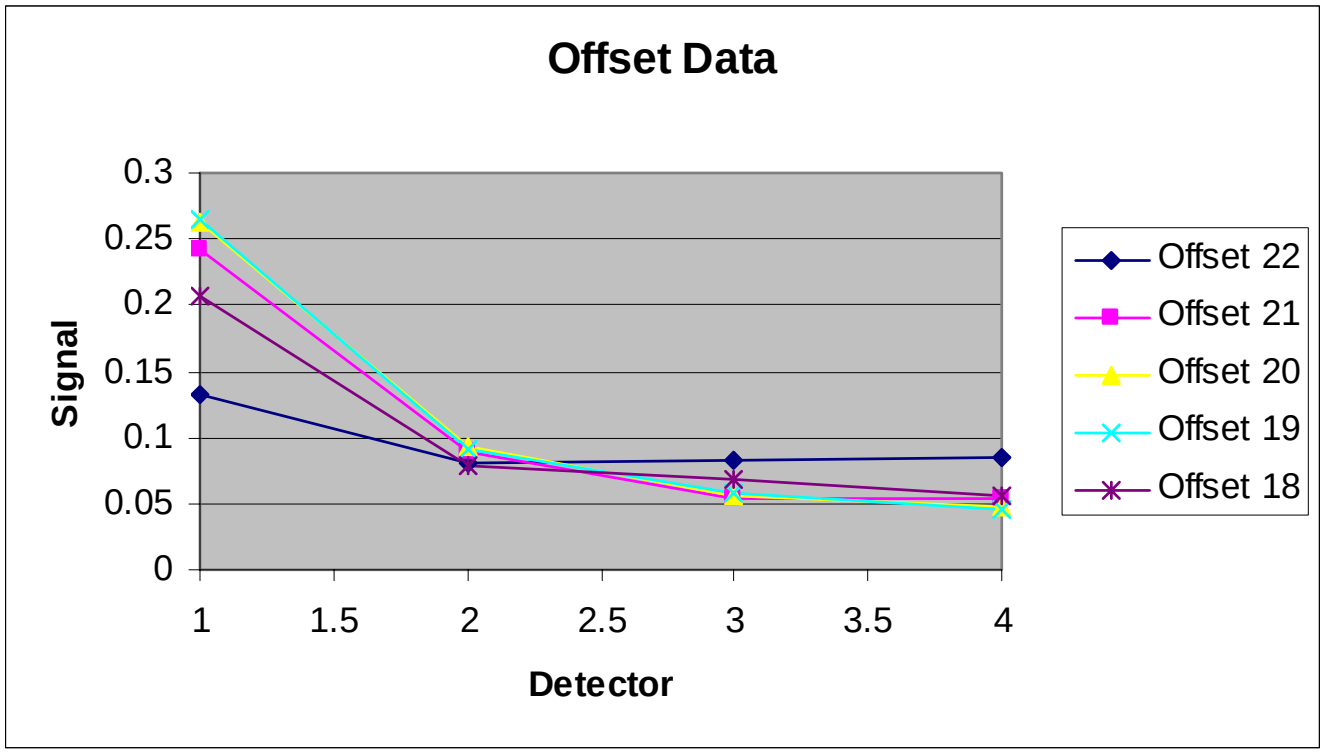
Offset Data
Signal
0.3
0.25
0.2
0.15
0.1
0.05
0
1
1.5
2
2.5
3
3.5
4
Detector
Offset 22
Offset 21
Offset 20
Offset 19
Offset 18

Appendix 3

	Phantom 1			
	D1	**D2**	**D3**	**D4**
S1	1.297139	0.39263	0.25359	0.13135
S4	1.365926	0.413901	0.263294	0.136812
Constant	1.05303	1.054176	1.038269	1.041589
	Phantom 2			
S1	0.941787	0.254124	0.146395	0.06923
S4	1.01503	0.279377	0.156344	0.071244
Constant	1.07777	1.099374	1.067958	1.029093
	Phantom 3			
S1	1.162936	0.352132	0.217853	0.112123
S4	1.282109	0.377096	0.234836	0.117617
Constant	1.102476	1.070894	1.077958	1.048994
Average	**1.077759**	**1.074815**	**1.061395**	**1.039892**
Variance	**0.000611**	**0.000522**	**0.000426**	**0.000101**

	Phantom 1			
	D1	**D2**	**D3**	**D4**
S2	0.222034	0.086061	0.061646	0.038773
S3	0.765942	0.252262	0.171557	0.096178
Constant	3.44966	2.931206	2.782923	2.480514
	Phantom 2			
S2	0.196414	0.077974	0.055406	0.033326
S3	0.750103	0.25301	0.168567	0.092332
Constant	3.818988	3.244809	3.042415	2.770598
	Phantom 3			
S2	0.214801	0.085832	0.061845	0.03769
S3	0.802411	0.276509	0.189761	0.105058
Constant	3.735598	3.221509	3.068344	2.787436
Average	**3.668082**	**3.132508**	**2.96456**	**2.679516**
Variance	**0.03752**	**0.030528**	**0.024912**	**0.029772**

Power calibration with Gold Standard Data

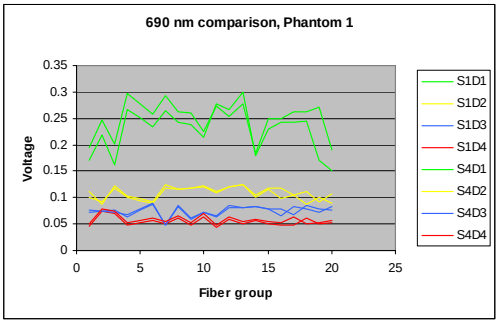

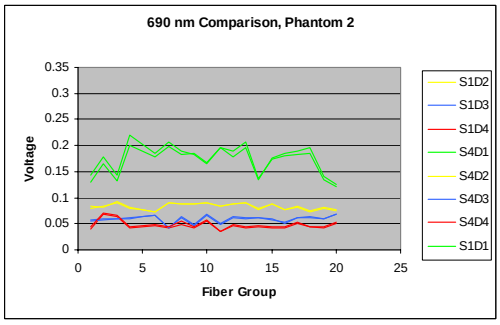

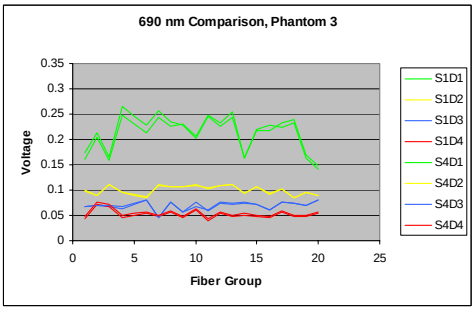

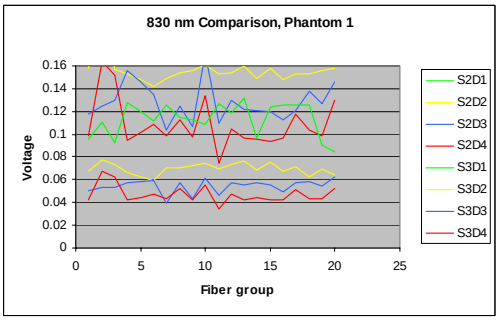

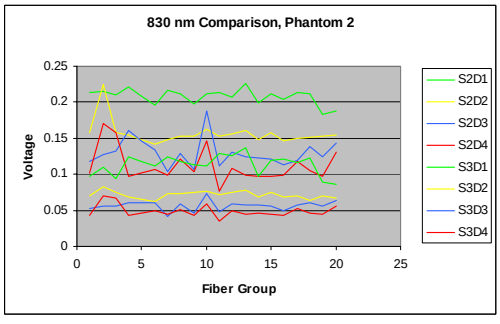

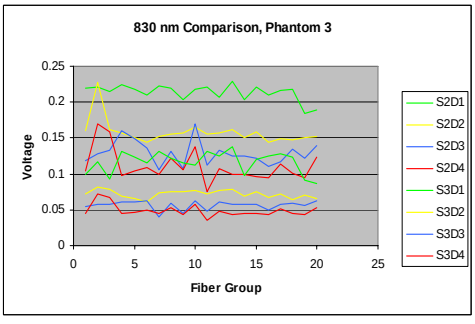

Appendix 4

	Phantom 1			
	D1	**D2**	**D3**	**D4**
S1	0.058091	0.050576	0.043183	0.040482
S4	0.113413	0.069524	0.054425	0.047135
Constant	1.95232	1.374644	1.260339	1.164343
	Phantom 2			
S1	0.056619	0.049928	0.043759	0.041733
S4	0.113272	0.071282	0.056352	0.048688
Constant	2.00061	1.427718	1.287769	1.166636
	Phantom 3			
S1	0.058148	0.050405	0.043572	0.041306
S4	0.116297	0.072068	0.056382	0.048878
Constant	2.000004	1.429798	1.293995	1.183318
Variance	**0.001469**	**0.00046**	**2.9E-05**	**0.000131**
Average	**1.031629**	**1.05601**	**1.067381**	**1.106296**

	Phantom 1			
	D1	**D2**	**D3**	**D4**
S2	0.231434	0.102811	0.070352	0.052464
S3	0.228584	0.106138	0.074655	0.058587
Constant	0.987687	1.032357	1.061164	1.116701
	Phantom 2			
S2	0.163943	0.077707	0.055302	0.044469
S3	0.171981	0.082483	0.059205	0.04865
Constant	1.049028	1.061464	1.070566	1.094021
	Phantom 3			
S2	0.200076	0.09263	0.065175	0.049409
S3	0.211715	0.099504	0.069764	0.054753
Constant	1.058172	1.07421	1.070413	1.108167
Variance	**0.000768**	**0.000977**	**0.000321**	**0.000107**
Average	**1.984311**	**1.41072**	**1.280701**	**1.171432**

Power calibration with Optical Switch Data

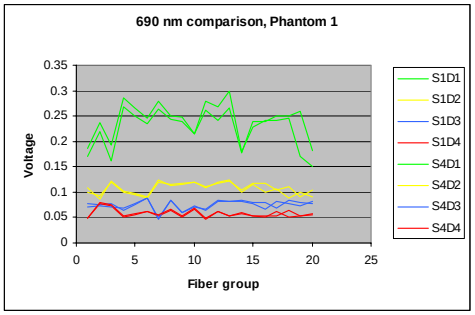

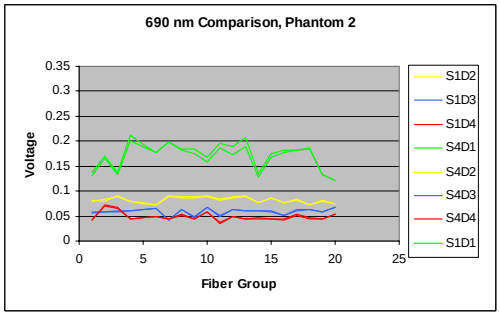

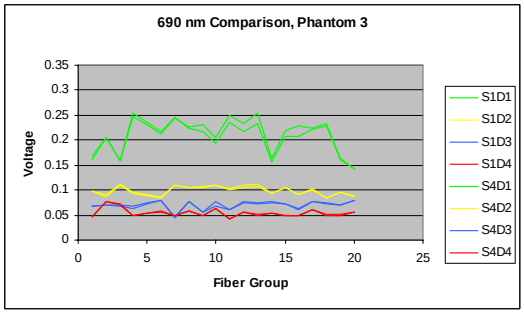

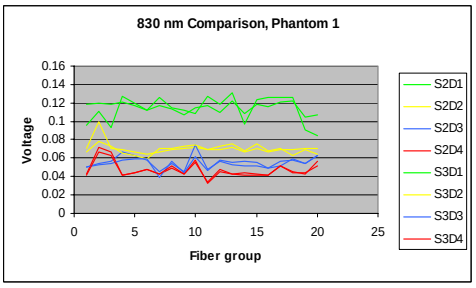

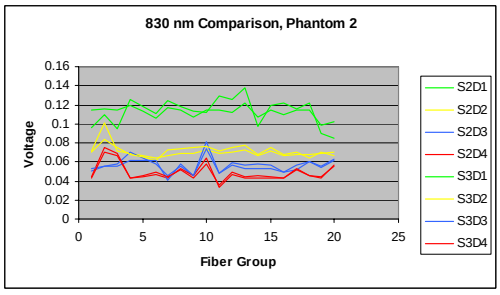

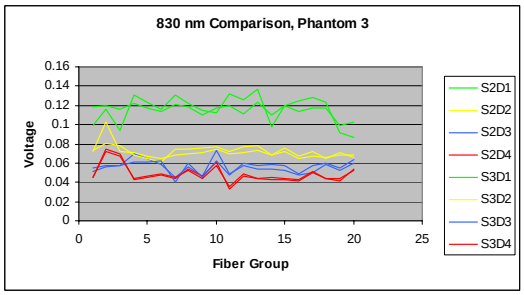

Appendix 5

	Source 1 Coefficients			
Fiber Group	D1	D2	D3	D4
1	1.271247	1.013631	1.022232	1.170696
2	1.021025	1.145606	1.008099	0.715651
3	1.282348	0.907677	0.999825	0.766656
4	0.831091	1.061732	1.082852	1.132872
5	0.898291	1.1178	0.969241	1.048312
6	0.977414	1.180125	0.880141	0.975645
7	0.868422	0.914577	1.522788	1.095703
8	0.952981	0.961188	0.924548	0.925433
9	0.978853	0.955543	1.258598	1.132258
10	1.101924	0.922974	0.947274	0.857569
11	0.916858	0.999365	1.183206	1.299831
12	0.995503	0.947633	0.939183	0.966212
13	0.910166	0.916105	0.968185	1.094093
14	1.359404	1.068264	0.948859	1.026937
15	1.021089	0.950345	0.982239	1.098372
16	0.997468	1.041895	1.093247	1.116226
17	0.955114	1.015421	0.987587	0.981186
18	0.935124	1.117052	0.933366	1.026388
19	1.194926	1.091069	0.991485	1.103013
20	1.421979	1.096624	0.912915	0.978248

	Source 2 Coefficients			
	D1	D2	D3	D4
1	0.960341	0.999365	1.096816	1.087466
2	0.951323	0.706821	1.017698	0.654753
3	0.972065	0.997421	0.980436	0.704405
4	0.932937	1.023048	0.813447	1.141024
5	0.975977	1.066948	0.879973	1.074781
6	1.023468	1.114793	0.958547	1.015977
7	0.952138	1.057962	1.239247	1.114058
8	0.977222	1.027256	1.011869	0.930635
9	1.043654	1.022062	1.209603	1.076569
10	0.977107	0.974944	0.734904	0.789819
11	0.964488	1.031523	1.16845	1.460769
12	1.015173	1.018807	0.984964	1.032905
13	0.919882	0.98452	1.047408	1.120311
14	1.038741	1.058961	1.059109	1.129802
15	0.96053	1.002364	1.068221	1.144291
16	0.997483	1.082051	1.152808	1.134697
17	0.957321	1.054544	1.088598	0.94484
18	0.956684	1.052398	0.945955	1.068676
19	1.120477	1.035965	1.041223	1.13801
20	1.088744	1.024296	0.908092	0.860675

	Source 3 Coefficients			
1	1.182013	1.014961	1.059442	1.111336
2	1.016814	0.879128	1.008663	0.689415
3	1.21967	0.941926	1.003811	0.73814
4	0.895122	1.050871	0.932909	1.121385
5	0.949739	1.106288	0.92215	1.052863
6	1.011463	1.167914	0.911754	0.992251
7	0.901726	0.980143	1.389288	1.099168
8	0.966526	0.976252	0.955436	0.927205
9	1.005344	0.955152	1.243996	1.118511
10	1.030422	0.935896	0.854888	0.844923
11	0.886888	0.999011	1.166931	1.370592
12	0.928302	0.946104	0.94465	0.999405
13	0.84537	0.913789	0.985268	1.109302
14	1.178055	1.040337	0.966953	1.065591
15	0.9454	0.940726	0.989693	1.105485
16	0.922929	1.048937	1.135222	1.129079
17	0.928161	0.997255	0.977249	0.929753
18	0.924736	1.112622	0.940419	1.084192
19	1.263563	1.018383	1.01162	1.101456
20	1.338136	1.082438	0.884915	0.904518

	Source 4 Coefficients			
1	1.339907	1.053597	1.054972	1.159201
2	1.051454	1.082791	1.014801	0.719138
3	1.36221	0.914443	1.02898	0.761364
4	0.86617	1.064746	1.037236	1.113427
5	0.925482	1.112563	0.949959	1.037109
6	0.993596	1.165063	0.878731	0.97069
7	0.878731	0.916932	1.489726	1.091359
8	0.951335	0.942375	0.920954	0.911594
9	0.946795	0.933098	1.242898	1.126886
10	1.052542	0.908888	0.986253	0.852559
11	0.863567	0.987268	1.160319	1.305869
12	0.905617	0.920031	0.921812	0.971146
13	0.822705	0.900637	0.954587	1.098942
14	1.292795	1.070635	0.939926	1.038763
15	0.99766	0.946979	0.993323	1.107809
16	0.953685	1.087908	1.139447	1.139229
17	0.957763	1.00954	0.940715	0.934749
18	0.937669	1.184275	0.954827	1.127372
19	1.324241	1.060151	1.012678	1.113765
20	1.490378	1.136541	0.893587	0.965156

Detector Normalization Coefficients

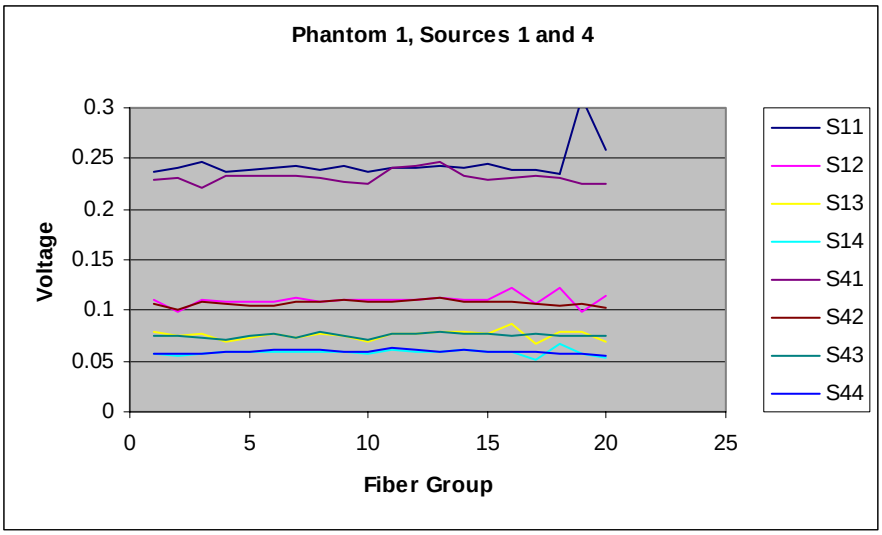
Phantom 1, Sources 1 and 4
Voltage
0.3
0.25
0.2
0.15
0.1
0.05
0
0
5
10
15
20
25
Fiber Group
S11
S12
S13
S14
S41
S42
S43
S44

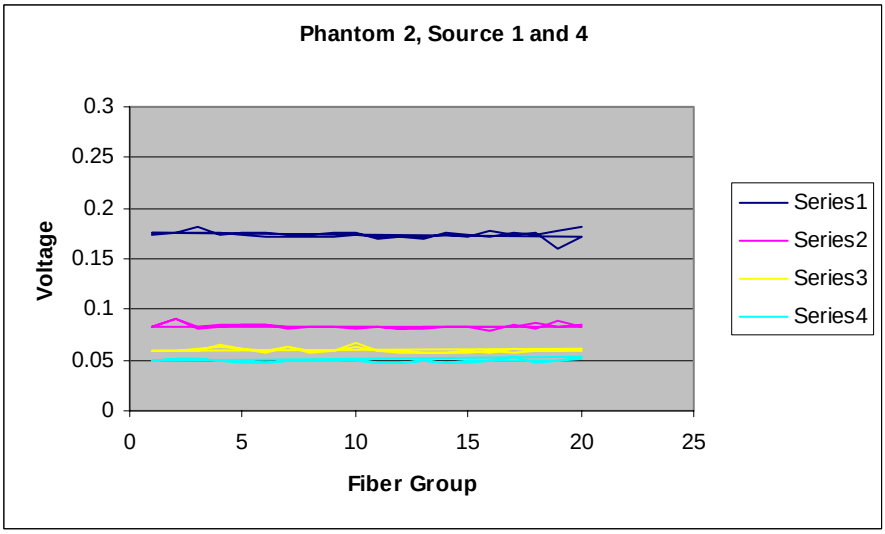
Phantom 2, Source 1 and 4
Voltage
0.3
0.25
0.2
0.15
0.1
0.05
0
0
5
10
15
20
25
Fiber Group
Series1
Series2
Series3
Series4

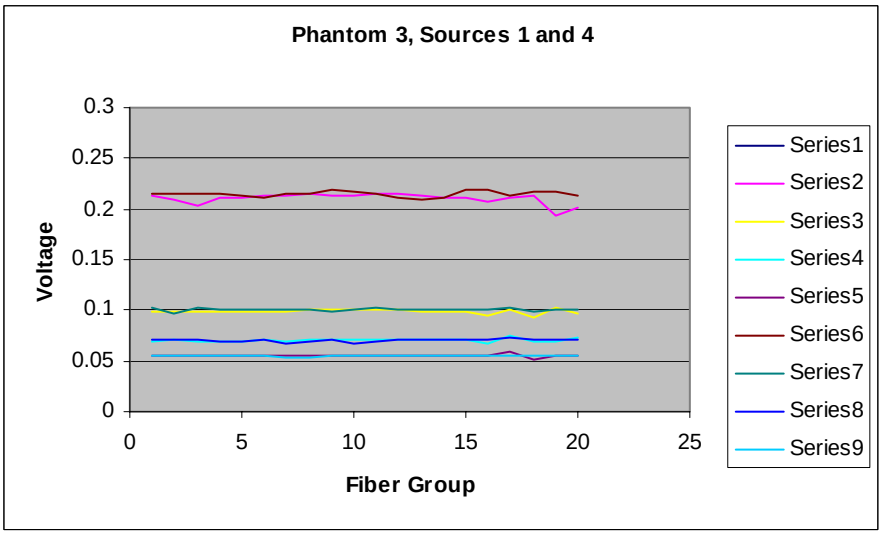
Phantom 3, Sources 1 and 4
Voltage
0.3
0.25
0.2
0.15
0.1
0.05
0
0
5
10
15
20
25
Fiber Group
Series1
Series2
Series3
Series4
Series5
Series6
Series7
Series8
Series9

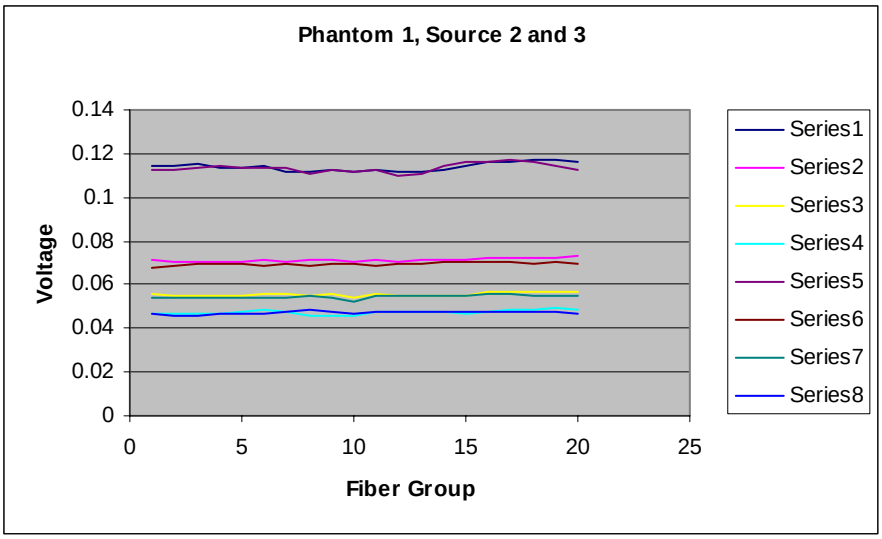
Phantom 1, Source 2 and 3
Voltage
0.14
0.12
0.1
0.08
0.06
0.04
0.02
0
0
5
10
15
20
25
Fiber Group
Series1
Series2
Series3
Series4
Series5
Series6
Series7
Series8

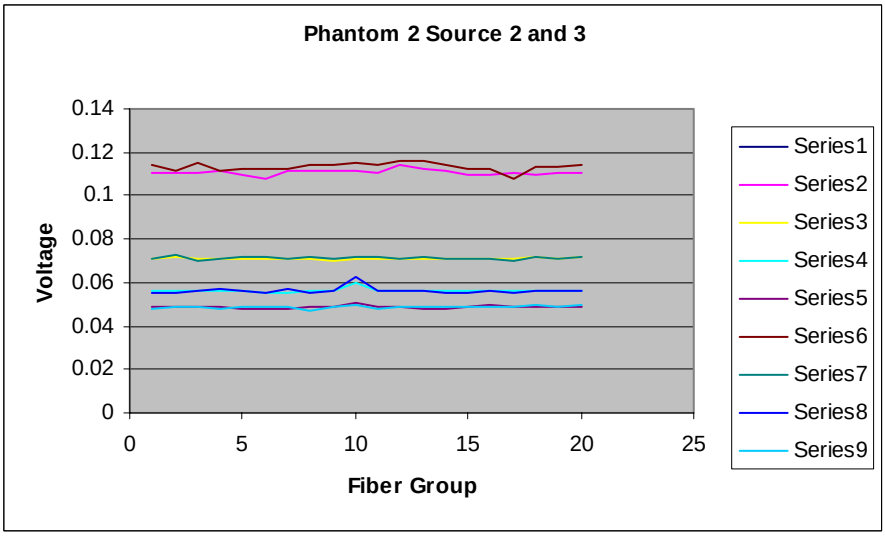
Phantom 2 Source 2 and 3
Voltage
0.14
0.12
0.1
0.08
0.06
0.04
0.02
0
0
5
10
15
20
25
Fiber Group
Series1
Series2
Series3
Series4
Series5
Series6
Series7
Series8
Series9

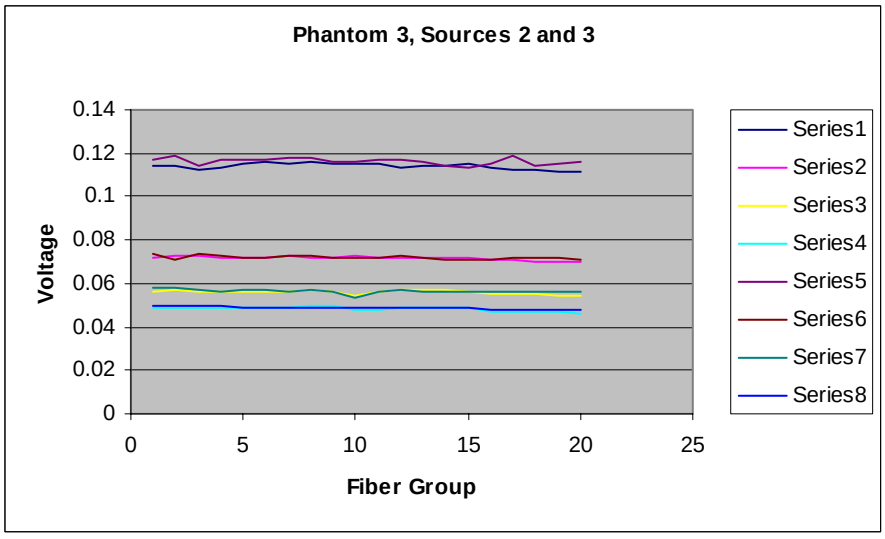
Phantom 3, Sources 2 and 3
Voltage
0.14
0.12
0.1
0.08
0.06
0.04
0.02
0
0
5
10
15
20
25
Fiber Group
Series1
Series2
Series3
Series4
Series5
Series6
Series7
Series8

Appendix 6

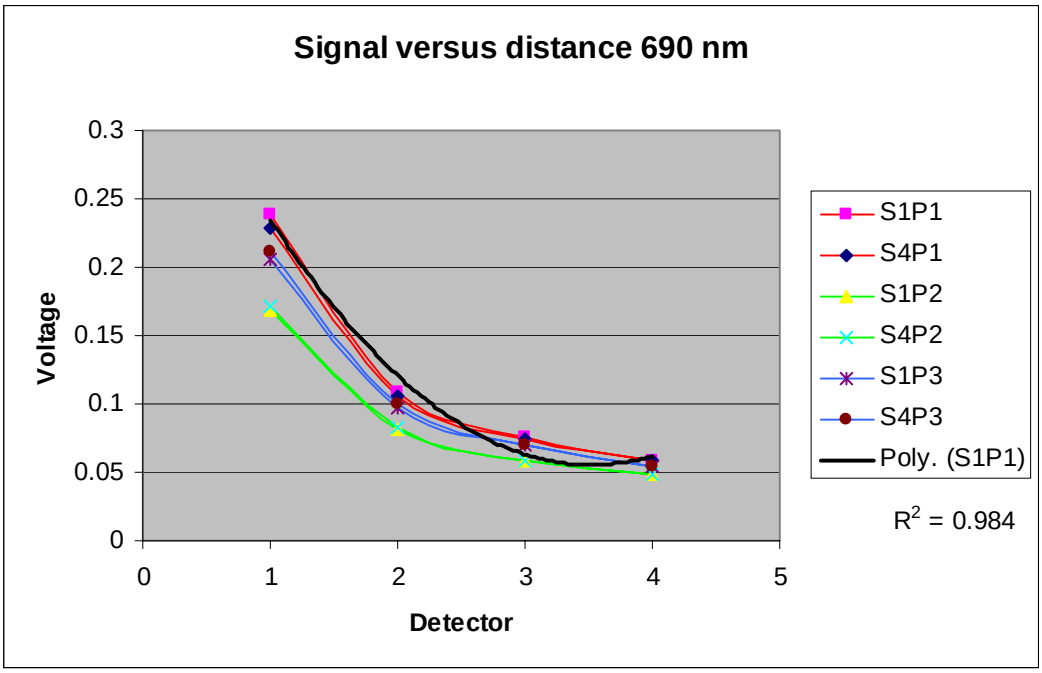
Signal versus distance 690 nm
Voltage
0.3
0.25
0.2
0.15
0.1
0.05
0
0
1
2
3
4
5
Detector
S1P1
S4P1
S1P2
S4P2
S1P3
S4P3
Poly. (S1P1)
R2 = 0.984

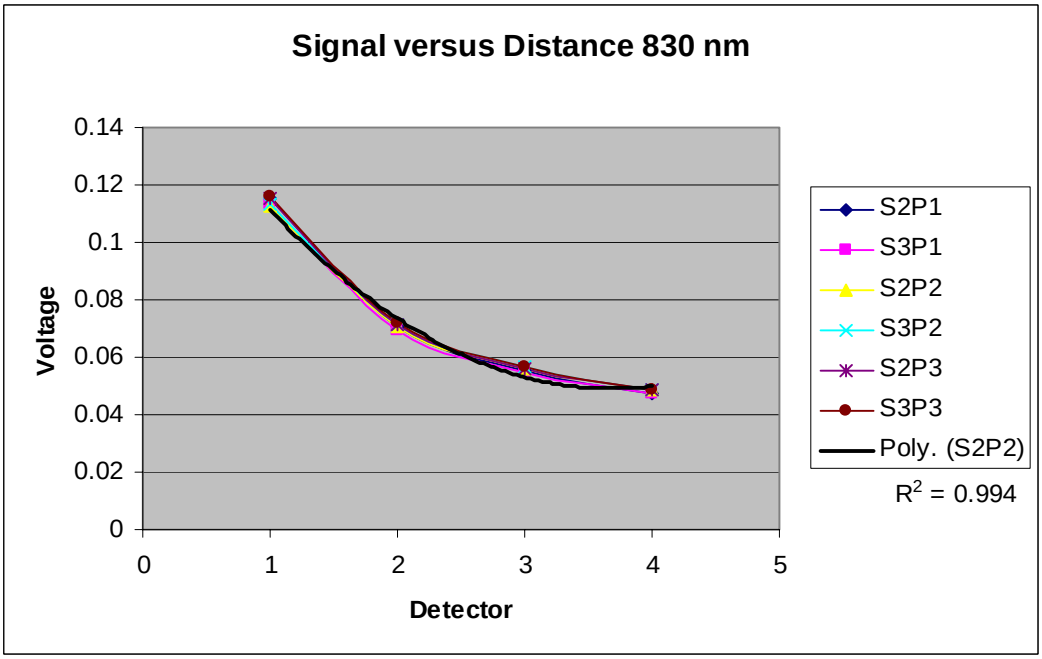
Signal versus Distance 830 nm
Voltage
0.14
0.12
0.1
0.08
0.06
0.04
0.02
0
0
1
2
3
4
5
Detector
S2P1
S3P1
S2P2
S3P2
S2P3
S3P3
Poly. (S2P2)
R2 = 0.994

	Source 1 Detector Comparison			
	D1:D1	D2:D1	D3:D1	D4:D1
P1	1	2.231989	3.230639	4.193463
P2	1	2.073286	2.890978	3.499483
P3	1	2.122436	2.993779	3.827588
average	1	2.14257	3.038465	3.840178
variance	0	0.006601	0.03034	0.120521
	Source 2 Detector Comparison			
	D1:D1	D2:D1	D3:D1	D4:D1
P1	1	1.595625	2.046713	2.400072
P2	1	1.560661	1.973323	2.275121
P3	1	1.587653	2.030589	2.358823
average	1	1.581313	2.016875	2.344672
variance		0.000336	0.001488	0.004053
	Source 3 Detector Comparison			
	D1:D1	D2:D1	D3:D1	D4:D1
P1	1	1.631127	2.083128	2.40375
P2	1	1.589903	2.012734	2.328534
P3	1	1.613446	2.060742	2.380212
	1	1.611492	2.052201	2.370832
variance		0.000428	0.001294	0.00148
	Source 4 Detector Comparison			
	D1:D1	D2:D1	D3:D1	D4:D1
P1	1	2.158657	3.072024	3.917831
P2	1	2.093346	2.92241	3.579885
P3	1	2.134391	3.05196	3.898452
average	1	2.128798	3.015464	3.798723
variance		0.00109	0.006595	0.036011

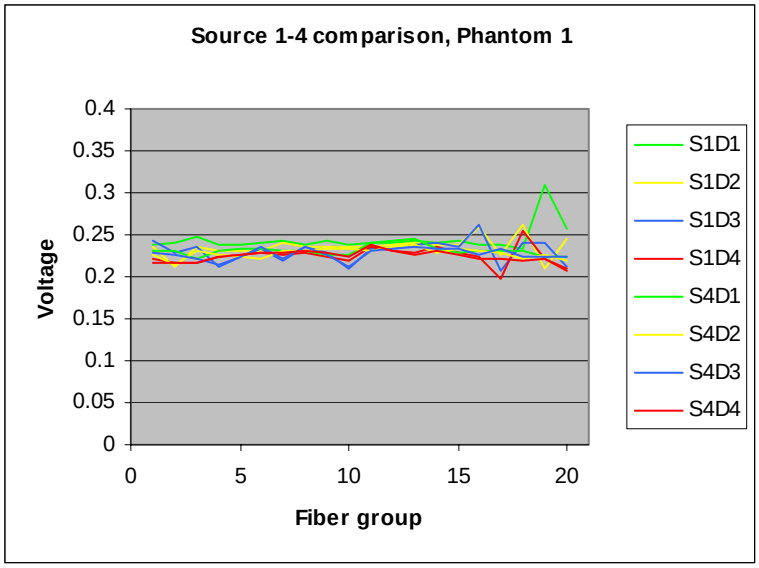
Source 1-4 comparison, Phantom 1
Voltage
0.4
0.35
0.3
0.25
0.2
0.15
0.1
0.05
0
0
5
10
15
20
Fiber group
S1D1
S1D2
S1D3
S1D4
S4D1
S4D2
S4D3
S4D4

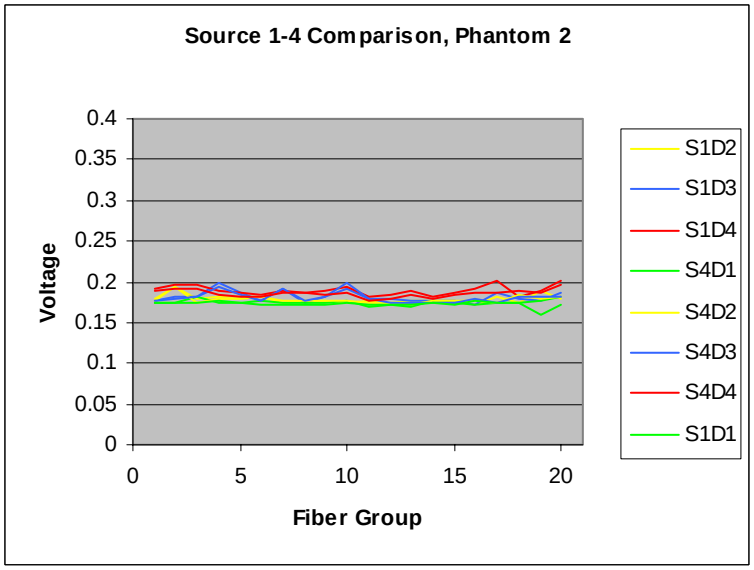
Source 1-4 Comparison, Phantom 2
Voltage
0.4
0.35
0.3
0.25
0.2
0.15
0.1
0.05
0
0
5
10
15
20
Fiber Group
S1D2
S1D3
S1D4
S4D1
S4D2
S4D3
S4D4
S1D1

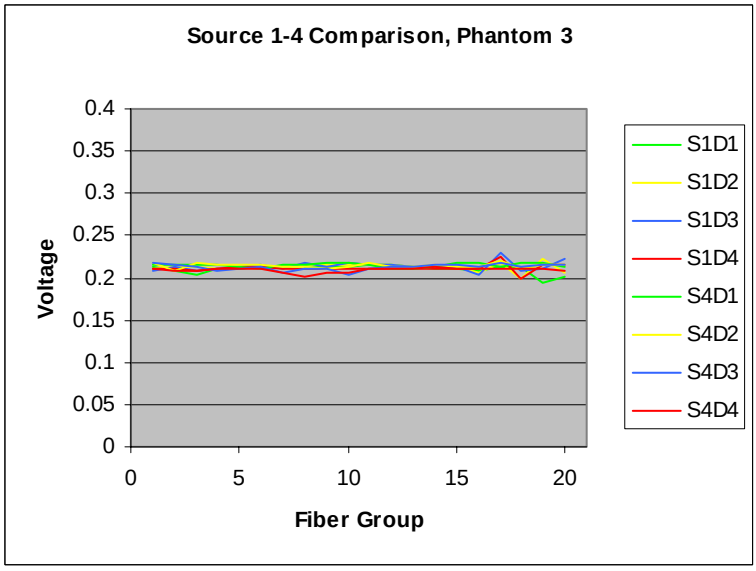
Source 1-4 Comparison, Phantom 3
Voltage
0.4
0.35
0.3
0.25
0.2
0.15
0.1
0.05
0
0
5
10
15
20
Fiber Group
S1D1
S1D2
S1D3
S1D4
S4D1
S4D2
S4D3
S4D4

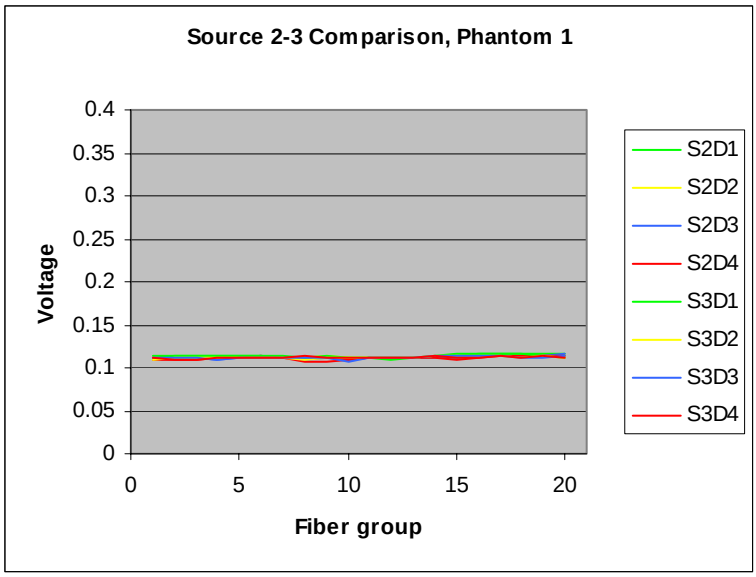
Source 2-3 Comparison, Phantom 1
Voltage
0.4
0.35
0.3
0.25
0.2
0.15
0.1
0.05
0
0
5
10
15
20
Fiber group
S2D1
S2D2
S2D3
S2D4
S3D1
S3D2
S3D3
S3D4

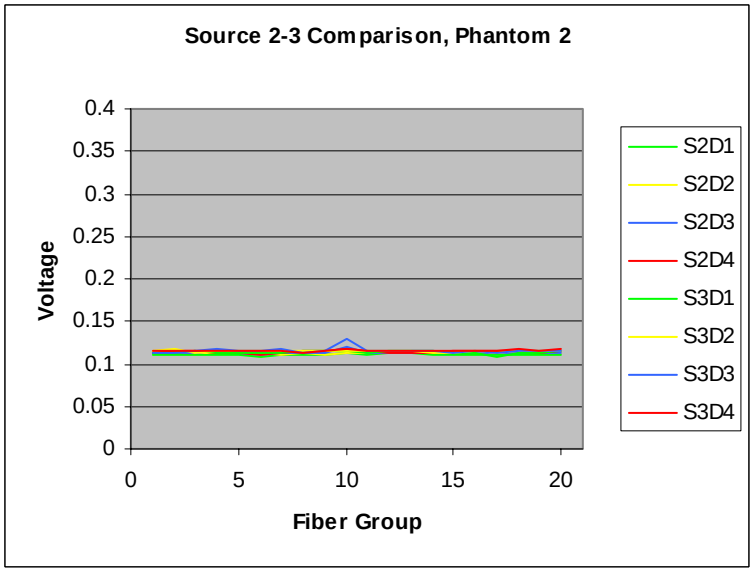
Source 2-3 Comparison, Phantom 2
Voltage
0.4
0.35
0.3
0.25
0.2
0.15
0.1
0.05
0
0
5
10
15
20
Fiber Group
S2D1
S2D2
S2D3
S2D4
S3D1
S3D2
S3D3
S3D4

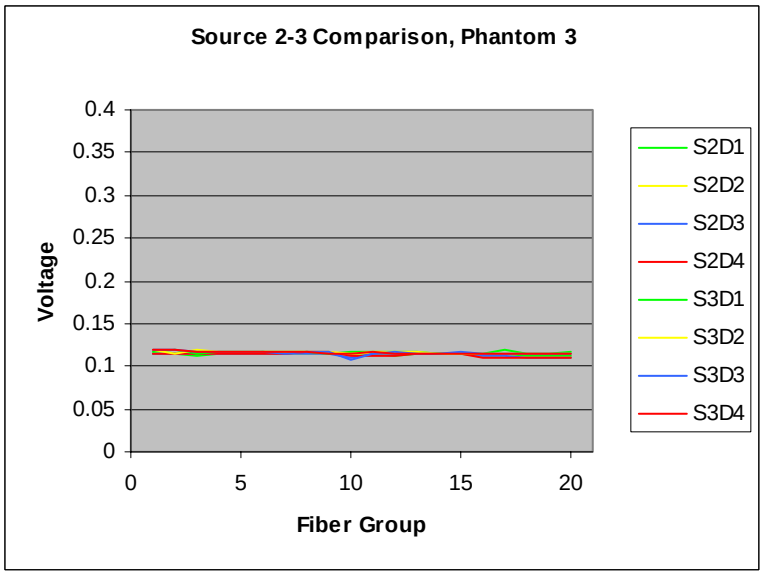
Source 2-3 Comparison, Phantom 3
Voltage
0.4
0.35
0.3
0.25
0.2
0.15
0.1
0.05
0
0
5
10
15
20
Fiber Group
S2D1
S2D2
S2D3
S2D4
S3D1
S3D2
S3D3
S3D4